CHALMERS
UNIVERSITY OF TECHNOLOGY

Efficient Calculation of the Lattice Thermal Conductivity by Atomistic Simulations with Ab Initio Accuracy

ADVANCED THEORY AND SIMULATIONS
www.advtheorysimul.com

Efficient Calculation of the Lattice Thermal Conductivity by Atomistic Simulations with Ab Initio Accuracy

*Joakim Brorsson, Arsalan Hashemi, Zheyong Fan, Erik Fransson, Fredrik Eriksson, Tapio Ala-Nissila, Arkady V. Krasheninnikov, Hannu-Pekka Komsa, and Paul Erhart**

High-order force constant expansions can provide accurate representations of the potential energy surface relevant to vibrational motion. They can be efficiently parametrized using quantum mechanical calculations and subsequently sampled at a fraction of the cost of the underlying reference calculations. Here, force constant expansions are combined via the HIPHIVE package with GPU-accelerated molecular dynamics simulations via the GPUMD package to obtain an accurate, transferable, and efficient approach for sampling the dynamical properties of materials. The performance of this methodology is demonstrated by applying it both to materials with very low thermal conductivity ($Ba_8Ga_{16}Ge_{30}$, SnSe) and a material with a relatively high lattice thermal conductivity (monolayer-MoS_2). These cases cover both situations with weak (monolayer-MoS_2, SnSe) and strong ($Ba_8Ga_{16}Ge_{30}$) pho renormalization. The simulations also enable to access complementary information such as the spectral thermal conductivity, which allows to discriminate the contribution by different phonon modes while accounting for scattering to all orders. The software packages described here are made available to the scientific community as free and open-source software in order to encourage the more widespread use of these techniques as well as their evolution through continuous and collaborative development.

1. Introduction

The lattice thermal conductivity (LTC) is a crucial quantity in the development of electronic and other functional devices, such as transistors,[1,2] thermoelectric materials,[3] and heat management systems.[4,5] Atomistic simulations are powerful tools to complement experimental investigations of the LTC, providing both valuable microscopic insight and quantitative predictions and guidance in the search for both ultra-high[6–9] and ultra-low LTC materials.[5,10–12] The two most common computational approaches are based on solving the Boltzmann transport equation (BTE) and on molecular dynamics (MD) simulations, respectively.

The BTE approach is founded in perturbation theory and requires knowledge of the low-order interatomic force constants (IFCs) that dominate thermal transport in many crystalline materials. The IFCs can often be computed with relatively small effort using quantum mechanical, most commonly density functional theory (DFT),

J. Brorsson
Department of Chemistry and Chemical Engineering
Chalmers University of Technology
Gothenburg SE-412 96, Sweden

E. Fransson, F. Eriksson, P. Erhart
Department of Physics
Chalmers University of Technology
SE-412 96 Gothenburg, Sweden
E-mail: erhart@chalmers.se

T. Ala-Nissila
QTF Centre of Excellence
Department of Applied Physics
Aalto University
P.O. Box 11100, Aalto 00076, Finland

A. Hashemi, Z. Fan, A. V. Krasheninnikov, H.-P. Komsa
Department of Applied Physics
Aalto University
P.O. Box 11100, Aalto 00076, Finland

Z. Fan
School of Mathematics and Physics
Bohai University
Jinzhou, Liaoning 121013, China

T. Ala-Nissila
Interdisciplinary Centre for Mathematical Modelling and Department of Mathematical Sciences
Loughborough University
Loughborough, Leicestershire LE11 3TU, UK

A. V. Krasheninnikov
Institute of Ion Beam Physics and Materials Research
Helmholtz-Zentrum Dresden-Rossendorf
Dresden 01328, Germany

H.-P. Komsa
Microelectronics Research Unit
University of Oulu
Oulu 90014, Finland

The ORCID identification number(s) for the author(s) of this article can be found under https://doi.org/10.1002/adts.202100217

DOI: 10.1002/adts.202100217

calculations. BTE calculations routinely include IFC terms terms up to third-order via packages such as PHONO3PY,[13] ALAMODE,[14] SHENGBTE,[15] QUANTUM ESPRESSO,[16] PHONTS,[17] or AAPL[18] and more recently also fourth-order terms.[7,19,20] The computational cost increases, however, steeply with increasing order, which makes this approach impractical, at least at present, for larger unit cells and/or lower-symmetry structures. For the BTE approach to work reliably, one requires the phonons to be proper quasi-particles, that is, the scattering rate should be (ideally much) smaller than the vibrational frequency. This limit can be violated, especially in materials with a very low LTC, which is often associated with short phonon lifetimes. While for some of these cases renormalized phonons and effective harmonic models have been employed with good success,[21,22] such techniques are demanding in terms of human effort and computer time. In this context, the unified lattice-dynamics approach is also promising as it connects the IFC-BTE framework to the Allen-Klein approach for glass-like conductors.[23]

The LTC can also be extracted from MD simulations using correlation functions as in the Green–Kubo approach[24,25] or specialized thermostats as in the homogeneous nonequilibrium molecular dynamics (HNEMD) approach.[26,27] MD simulations have the principal advantage of not imposing any limit on the order of the scattering process, while being equally applicable to crystalline and amorphous materials, and making no distinction between crystalline and glass-like conduction. They do not naturally account for quantum effects, which can be a limitation at low temperatures. In practice their applicability is, however, more severely restricted by the availability of suitable force fields. As a result, most MD studies of the LTC to date have been conducted using empirical potentials, which are only available for a rather limited set of materials and differ widely with respect to their suitability for this task.

More recently Green–Kubo approaches have been also adapted to ab initio MD simulations, commonly based on DFT.[28,29] Unfortunately, due to the very high cost of DFT compared to interatomic potentials such approaches can be limited with respect to system size and complexity. In addition, it can be difficult to achieve convergence as this can require multiple sampling on rather long time scales (also see below). A middle ground is provided by machine learning (ML) potentials, which promise to bridge between the accuracy of DFT and the computational efficiency of empirical potentials. For this approach to be effective, one requires a facile scheme for constructing potentials that requires as little input data and as little supervision as possible. For the specific purpose of analyzing the dynamics of materials and in particular the LTC, high-order force constant potentials (FCPs) can now be routinely constructed even for materials with large unit cells, low symmetry, and soft interactions.[21,30–37]

FCPs offer several advantages that are worth emphasizing. They are flexible, allowing the description of a wide range of systems, and extensible as they can, given enough data, describe many-body effects up to any order. They are easy to construct since they are linear models for which fitting is very well understood and require relatively small amounts of training data, especially compared to general ML potentials. Moreover, they are convenient in so far as their low-order limit is well understood in the context of the harmonic approximation and perturbation theory. Thus implementing an efficient calculator for FCPs serves multiple purposes as they not only provide a general functional form for interatomic potentials of solids, but they also connect BTE and MD approaches.

A further improvement can be achieved by accelerating the calculations using graphics processing units (GPUs). While the potential benefit of this approach has been demonstrated already in ref. [32] to the best of our knowledge there exists no generally accessible implementation. We have therefore implemented FCPs in GPUMD using the HIPHIVE package for FCP construction, both of which are publicly available as free and open source software (FOSS). Here, we demonstrate and benchmark this approach. The GPU-accelerated implementation achieves a speedup by a factor of at least 30 to 40 for the cases considered here, equivalent to a reduction in wall-time from over a day to about half an hour for a typical simulation. This provides one with a workflow that allows for MD simulations with DFT quality forces at nanosecond time scales using models that can be constructed with semi-automatized protocols with very little training data.

The next section provides an overview of the protocol used here and summarizes the key aspects of the methodology. In particular, we discuss strategies for selection and/or generation of reference structures for the construction of FCPs. In Section 3, we consider three materials with varying degrees of anharmonicity that correspond to an intermediate LTC with a temperature dependence typical of crystalline semiconductors (monolayer-MoS_2 or ml-MoS_2) and very low LTCs at the threshold of glass-like conduction ($Ba_8Ga_{16}Ge_{30}$, SnSe). This includes an analysis of the efficacy of different MD methods for computing the LTC as well as a convergence study of several important simulation parameters. By making this methodology widely available, we hope to enable the widespread use of this approach both for the calculation of the LTC but more generally for the analysis of dynamical properties of crystalline materials. For this reason we have made the data presented in this study publically available.[70] We also note that much more extensive analyses can be readily carried out on the basis of MD trajectories, such as free energy calculations and analysis of correlation functions.

2. Methodology

2.1. Overview

A workflow for the systematic analysis of dynamical properties, including the LTC, must handle (1) the construction of a FCP and (2) its subsequent sampling via MD simulations (**Figure 1**). A suitable starting point to accomplish the first task is a set of rattled structures, which can be generated by applying some form of random displacements (in the first iteration) or via MD simulations (in subsequent iterations). The reference forces for these structures, which can be routinely obtained from DFT calculations, are subsequently used to train a FCP, which we here handle via the HIPHIVE code.[34] The FCP can be iteratively improved by generating new representative configurations, for example, by running short MD simulations for small cells (typically not GPU accelerated), and feeding these back into the DFT code to generate more reference data.

Once a satisfactory FCP has been obtained, it can be fed into GPUMD, enabling very fast and efficient sampling of the relevant phase space. The output from these simulations typically consists

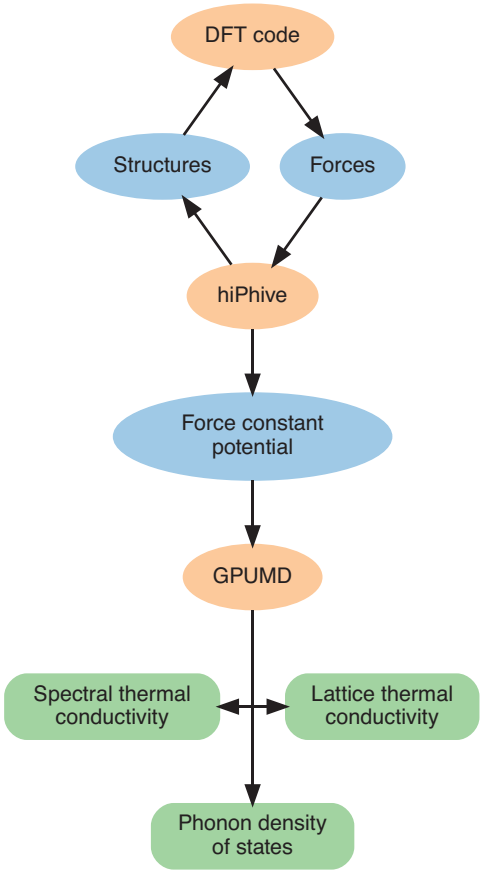

Figure 1. Schematic of workflow from FCP construction via MD simulations to various output quantities.

of the LTC and, if requested, the spectral thermal conductivity or the (fully anharmonic) phonon density of states (PDOS). Additional information can be obtained by further analyzing the positions and velocities, yielding, for example, correlation functions and dynamical structure factors,[38] which provide in-depth information concerning the dynamics of the material and can also establish a direct connection to inelastic neutron or X-ray scattering experiments.

2.2. Strategies for the Construction of Force Constant Potentials

The potential energy surface can be expanded in a Taylor series with respect to the atomic displacements $\boldsymbol{u}$, relative to a set of reference positions $\boldsymbol{R}_0$

$$V = V_0 + \sum_i \sum_\alpha \Phi_i^\alpha u_i^\alpha + \underbrace{\frac{1}{2!}\sum_{ij}\sum_{\alpha\beta}\Phi_{ij}^{\alpha\beta}u_i^\alpha u_j^\beta}_{V_2} + \underbrace{\frac{1}{3!}\sum_{ijk}\sum_{\alpha\beta\gamma}\Phi_{ijk}^{\alpha\beta\gamma}u_i^\alpha u_j^\beta u_k^\gamma}_{V_3} + \underbrace{\frac{1}{4!}\sum_{ijkl}\sum_{\alpha\beta\gamma\eta}\Phi_{ijkl}^{\alpha\beta\gamma\eta}u_i^\alpha u_j^\beta u_k^\gamma u_l^\eta}_{V_4} + \cdots \quad (1)$$

where Φ are the IFCs, while the Latin and Greek indices enumerate atoms and Cartesian coordinates, respectively.

The first term in Equation (1) corresponds to a fixed shift of the potential and can be set to zero. If the reference positions $\boldsymbol{R}_0$ are taken as the equilibrium positions at zero temperature, the second term vanishes as well. Given these simplifications, the force acting on atom i along direction α is

$$F_i^\alpha = -\frac{\partial V}{\partial u_i^\alpha} = -\sum_j \sum_\beta \Phi_{ij}^{\alpha\beta} u_j^\beta - \frac{1}{2!}\sum_{jk}\sum_{\beta\gamma}\Phi_{ijk}^{\alpha\beta\gamma}u_j^\beta u_k^\gamma - \frac{1}{3!}\sum_{jkl}\sum_{\beta\gamma\eta}\Phi_{ijkl}^{\alpha\beta\gamma\eta}u_j^\beta u_k^\gamma u_l^\eta + \cdots \quad (2)$$

There are different aspects to consider when constructing FCPs, depending on the intended application. In broad terms, one could aim to construct harmonic FCPs for the analysis of thermodynamic properties (e.g., the free energy of a defective system), third-order and possibly fourth-order FCPs for BTE calculations or general higher-order FCPs for MD simulations. In the first two cases, it is typically sufficient to remain in the small displacement limit and one can generate training data by applying small normally identically independently distributed (i.i.d.) displacements. In the case of general higher-order FCPs several different strategies are available for composing training sets, three of which are considered in this work. Finally, there is the question of the optimization algorithm, which we extensively discussed in ref. [35].

2.2.1. Structure Generation by MD Simulations

The possibly most obvious yet not necessarily most efficient approach is to run (short) MD simulations using the reference method (commonly DFT), select a number of structures from the trajectory and use these for training. This approach, used below for $Ba_8Ga_{16}Ge_{30}$, has the immediate appeal of simplicity and ensuring by construction that the structures represent physically sound displacements. It is, however, computationally costly and as a result can suffer from an insufficient exploration of the energy landscape.

2.2.2. Structure Generation by Superimposing Normal Modes

To reduce the number of reference calculations one could imagine applying simply larger random displacements. This approach, however, yields very short interatomic distances, leading to very large repulsive forces and a very poor sampling of the relevant configuration space. A more elegant approach is to use a (possibly rough) estimate for the second-order IFCs to obtain a set of normal modes, which can be subsequently randomly populated with an average energy of $k_B T/2$ to generate physically sensible displacement patterns.[39] Compared to the approach based on explicit MD simulations, this method constitutes a considerable reduction in the number of reference calculations, as demonstrated for the case of MoS_2 below.

2.2.3. An Iterative Approach to Structure Generation

Neither of the two aforementioned approaches hedges against instabilities in the expansion that are known to be potential

pitfalls for strongly anharmonic materials.[35,36,40] To overcome this difficulty previous authors suggested to combine a regular FCP with empirical potentials.[36,40] Here, we describe a simple iterative approach that relies solely on the selection of reference structures and does not require additional terms in the energy expression. It thereby maintains the appealing simplicity and benefits of a pure FCP, allowing, for example, the separation of contributions by order; it can still be combined with empirical potentials if deemed desirable.

The iterative approach commences with the construction of an initial harmonic model based on small i.i.d. displacements. The resulting zeroth-generation FCP is used to generate structures by superimposing normal modes, for which reference forces are calculated. The latter are then used to construct the first anharmonic FCP including anharmonic terms up to even order and using, for example, the cutoff selection strategy outlined above. Then MD simulations are carried out using the first-generation FCP. Once these simulations fail (which is commonly the case for strongly anharmonic materials and/or small training sets), one or several of the structures leading up to the instability are selected for more reference calculations. Adding these data to the training set, a second-generation FCP is constructed, using which new MD simulations are carried out. This procedure is repeated iteratively and optionally for increasing temperatures in the MD simulations until a sufficiently stable FCP is obtained. It is important to emphasize that for any anharmonic force constant expansion one can trivially construct displacement patterns that are unstable. These conditions, however, correspond to unphysically large displacements, typically of only one or two atoms. One must hence ensure either by obtaining physically sound high-order terms or adding explicit repulsive terms that these conditions are not met. The iterative scheme outlined above and demonstrated below for the case of SnSe accomplishes this up to the temperatures of interest in this work.

2.3. Construction of Force Constant Potentials Using Hiphive

For $Ba_8Ga_{16}Ge_{30}$ we adopted the approach described in Section 2.2.1 using structures from DFT-MD simulation to construct a FCP for the ground state structure described in ref. [41]. To avoid additional convergence studies, we used the same cutoffs as for "Model 5" from ref. [35]. The model thus includes second-, third-, and fourth-order interactions up to 5.4 Å, 4.7 Å and 4.7 Å and has a total of more than 6000 parameters. The parameters were trained by ordinary least squares and 400 samples from DFT-MD simulations using the HIPHIVE package.[34] The DFT calculations were carried out for the 54-atom primitive unit cell using the VASP code[42] with the vdW-DF-cx exchange-correlation (XC) functional,[43,44] a plane wave energy cutoff of 319 eV, and a $3 \times 3 \times 3$ $\boldsymbol{k}$-point mesh. The classical equations of motion were integrated using a MD time step of 5 fs for a total simulated time of 25 ps following a 2.5 ps equilibration phase.

For ml-MoS_2 we adopted the approach described in Section 2.2.2 using structures obtained by superimposing normal models to construct a FCP. Reference forces were obtained by DFT calculations using the Perdew–Burke–Ernzerhof (PBE)[45] XC functional, a plane wave energy cutoff of 500 eV and a $15 \times 15 \times 1$ $\boldsymbol{k}$-point mesh. We generated 14 input structures based on $9 \times 9 \times 1$ supercells by superimposing normal modes with random phase factors and amplitudes corresponding to 300 K, 400 K, 500 K and 600 K. For comparison, the calculation of the IFCs up to third order using the direct method requires one to compute forces for at least 324 structures.[34] As the computational cost of FCP construction is almost entirely due to the DFT reference calculations, this approach to FCP construction corresponds to a reduction of the computational effort by more than a factor of 20. Using the reference data, we studied the convergence of FCP models with cutoff for increasing order (Figure S1). For the final model we used the cutoffs that minimized the cross-validated root-mean-square error (RMSE) over the validation set (Figure S1). The cross-validated RMSE quickly drops off as higher orders are included in the model and only decreases modestly beyond the fourth order (inset in **Figure 2**). A more detailed discussion of this cutoff-selection approach for FCP construction and its benefits can be found in ref. [35]. Lastly, rotational sum rules were enforced for the second-order IFCs, which is crucial step in order to obtain the correct quadratic phonon dispersion in 2D materials.

For SnSe we adopted the approach described in Section 2.2.3, using an iterative approach for generating training structures in order to obtain a stable FCP. In each iteration step, MD simulations were run at temperatures between 100 and 600 K using $2 \times 4 \times 4$ supercells, and 5 to 10 new training structures were selected from the trajectory just prior to the instability in the MD simulations. After 7 iterations, we obtained a total of 65 training structures from which the final FCP was trained which was found to be stable in MD simulations for the full temperatures range considered in the present work. For comparison, the direct enumeration approach to generate the IFCs up to only third order using, for example, PHONO3PY as in ref. [46] requires more than 2800 structures when using $3 \times 1 \times 1$ supercells and more than 9700 structures when using $2 \times 4 \times 4$ supercells. For this case, the computational cost associated with the DFT calculations is thus reduced by a factor of at least 40.

For computational efficiency it is useful to limit the number of FCP parameters, which both reduces file sizes and speeds up the calculations. For this reason, we removed all nth-order IFCs components with magnitudes below 10^{-8} eV Å^{-n}. This step has a minimal effect on the comparison of the forces predicted by the FCP and the reference forces from DFT calculations (Figure 2) as well as the fulfillment of the translational and rotational sum rules.

2.4. Thermal Conductivity from MD Simulations

After obtaining the FCPs, we calculate the LTC by running classical MD simulations via the equilibrium molecular dynamics (EMD) and HNEMD methods, respectively. In the EMD approach, the thermal conductivity tensor $\kappa^{\alpha\beta}(t)$, which is a function of the correlation time t, is calculated as a time integral of the heat current autocorrelation function $\langle J^{\alpha}(0)J^{\beta}(t)\rangle$ according to the Green–Kubo relation for heat transport[24,25]

$$\kappa^{\alpha\beta}(\tau) = \frac{1}{k_{\mathrm{B}} T^2 V} \int_0^{\tau} dt' \left\langle J^{\alpha}(0) J^{\beta}(t') \right\rangle \tag{3}$$

Here, k_{B} is the Boltzmann constant, V is the volume of the simulated system, and T is the absolute temperature. The angular

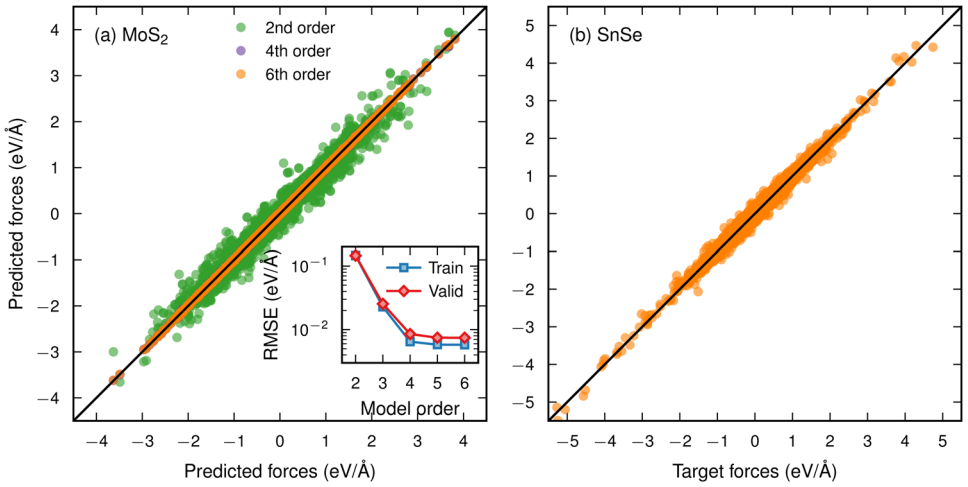

Figure 2. Comparison of predicted (FCP) and target (DFT) force components in a) ml-MoS_2 and b) SnSe. The inset shows the root mean square error (RMSE) obtained by cross-validation for training (blue squares) and validation (red diamonds) sets as a function of expansion order.

brackets in the heat current autocorrelation function denote an ensemble average, which is approximated as a time average in MD simulations. Similar to the potential energy and the interatomic force, the total heat current in the system, $\boldsymbol{J}$, can also be expressed in terms of the IFCs. Following the derivations in refs. [47, 48] we have

$$J^{\delta} = \sum_{i} J_{i}^{\delta} = \sum_{i} \sum_{\alpha} W_{i}^{\delta\alpha} v_{i}^{\alpha} \tag{4}$$

where v_i^{α} is the velocity in the direction α for particle i and $W_i^{\delta\alpha}$ is the $\delta\alpha$ component of the virial

$$W_{i}^{\delta\alpha} = \frac{1}{2!} \sum_{j} \sum_{\beta} r_{ij}^{\delta} \Phi_{ij}^{\alpha\beta} u_{j}^{\beta} + \frac{2}{3!} \sum_{jk} \sum_{\beta\gamma} r_{ij}^{\delta} \Phi_{ijk}^{\alpha\beta\gamma} u_{j}^{\beta} u_{k}^{\gamma} + \frac{3}{4!} \sum_{jkl} \sum_{\beta\gamma\eta} r_{ij}^{\delta} \Phi_{ijkl}^{\alpha\beta\gamma\eta} u_{j}^{\beta} u_{k}^{\gamma} u_{l}^{\eta} + \cdots \tag{5}$$

Here, $r_{ij}^{\delta} \equiv r_{j}^{\delta} - r_{i}^{\delta}$ is the δ-component of the distance vector between particles i and j. While a convective heat transfer term can also be included, it is negligible in stable solids and is therefore not considered here. We have validated the above heat current formula using energy conservation in non-equilibrium MD simulations, similar to the approach in the previous work.[49,50]

Ladd et al.[51] have found that the third-order heat current is non-negligible for argon, modeled using a Lennard-Jones potential, at relatively high temperatures (close to the melting point). For the systems considered here the results obtained by considering only the harmonic (first term in Equation 5) heat current agree within the error bars with those obtained by including both harmonic and third-order (second term in Equation 5) heat currents up to the statistical accuracy achievable in our MD simulations (**Figure 3**). For the sake of computational efficiency, we therefore did not include heat currents beyond the third order in the HNEMD and EMD simulations described below.

The HNEMD method (see ref. [52]) is physically equivalent to the EMD method as it is also based on the Green–Kubo relation for the LTC.[26,27,52] In the former case, however, a non-equilibrium steady state is generated by adding an external driving force on every particle in the system[48,52]

$$F_{i}^{\alpha} \rightarrow F_{i}^{\alpha} + \sum_{\delta} F_{e}^{\delta} W_{i}^{\delta\alpha} \tag{6}$$

Here, F_e^{δ} is the δ component of the driving force parameter, which has the dimension of inverse length. It should be small enough to keep the system within the linear response regime, as discussed further in Section 3. The resulting nonzero heat current $\langle J^{\alpha}(t) \rangle_{\mathrm{ne}}$ is proportional to the magnitude of the driving force, if the latter is small enough for the system to remain in the linear response regime,

$$\frac{\langle J^{\alpha}(t) \rangle_{\mathrm{ne}}}{TV} = \sum_{\beta} \kappa^{\alpha\beta}(t) F_{e}^{\beta} \tag{7}$$

where the proportionality coefficient corresponds to the components of the LTC tensor. To examine the convergence of the LTC with respect to simulation time, it is useful to consider the time average, which is defined as[52]

$$\bar{\kappa}^{\alpha\beta}(t) = \frac{1}{t} \int_{0}^{t} dt' \frac{\langle J^{\alpha}(t') \rangle_{\mathrm{ne}}}{TVF_{e}^{\beta}} \tag{8}$$

where we assumed that F_e^{β} is non-zero along only one direction (which is easily realized in practice). The choice of the driving force F_e is discussed in ref. [52], according to which a hard condition for F_e is $\lambda_{\max} F_e \leq 1$. Although one does not know $\lambda_{\max}$ for a material a priori, one knows that it decreases with increasing temperature. Therefore, if F_e is small enough for a given temperature, it must be small enough for higher temperatures. The choice of F_e can be compared to the choice of the integration time step in MD simulations. Its effect should be tested for the specific system of interest and prior experience is valuable.

In the HNEMD formalism, the LTC can be conveniently resolved with respect to the phonon frequency ω[48,52] via the

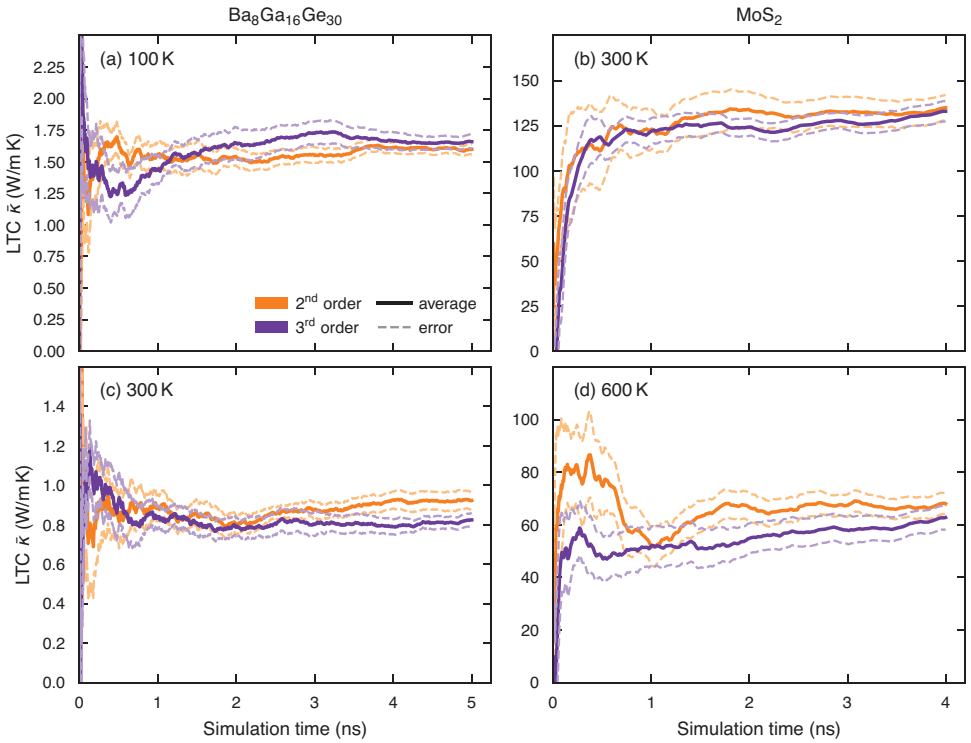

Figure 3. Contributions to the lattice thermal conductivity (LTC) resulting from the heat current up to second and third order, respectively, (see Equation 5) from HNEMD simulations for a,c) $Ba_8Ga_{16}Ge_{30}$ and b,d) ml-MoS_2.

spectral thermal conductivity

$$\kappa^{\alpha\beta}(\omega) = \frac{2}{TVF_e^{\beta}} \int_{-\infty}^{\infty} K^{\alpha}(t) e^{i\omega t} dt \tag{9}$$

where

$$K^{\alpha}(t) = \sum_j \left\langle \sum_{\delta} W_j^{\alpha\delta}(0) v_j^{\delta}(t) \right\rangle_{\text{ne}} \tag{10}$$

is the virial–velocity correlation function evaluated via nonequilibrium ensemble averaging during the HNEMD simulation.

We have implemented both the EMD and HNEMD methods for FCPs in the GPUMD package[53] (GPUMD-v2.5.1), which is a high-performance MD code fully implemented on GPUs. We carefully checked that the forces computed from GPUMD agree with those from HIPHIVE up to machine precision for each of the systems under consideration.

For all methods and systems, we applied a 1 fs time step and equilibrated the systems in the *NVT* ensemble for 1 ns before the LTC production runs. When using the EMD method, we then sampled the system in the *NVE* ensemble, whereas when using the HNEMD approach the system was subjected to an external driving force F_e^{α} according to Equation 6. We note that in these simulations we neglect the effect of thermal expansion. This approximation is widely used in calculations of the LTC, in particular when using the BTE, and is motivated by the observation that temperature usually has a far stronger impact on phonon dispersion and lifetimes than thermal expansion.

2.5. Comments on the EMD and HNEMD Techniques

It is instructive to briefly recapitulate the similarities and differences between the EMD and HNEMD. Interested readers will find more information on this topic in the literature.[50,52,54–56]

In the EMD approach one exploits the fluctuation–dissipation theorem to infer the LTC from *equilibrium simulations* via the Green–Kubo relation for the LTC. For this approach to work well, one hence needs to converge the heat current correlation function as a function of correlation time τ, see Equation 3. Since the correlation time increases with the LTC, this method can become computationally increasingly demanding for materials with a high LTC. It is also noteworthy that the EMD approach (unlike the HNEMD approach) allows one in principle to obtain all the components of the LTC tensor from a single set of simulations.

The HNEMD method subjects the system to an external driving force and allows one to accurately extract the LTC from *nonequilibrium simulations* provided the response remains in the linear regime. Unlike in the EMD approach, the LTC is obtained as an average in simulation time, see Equation 8. As a result, the HNEMD approach in the limit of vanishing driving force ($F_e \to 0$) does not become identical to the EMD. Rather, as evident from Equation 8, the numerical convergence of the expression for the LTC worsens. Thus the HNEMD approach requires a judicious choice of the driving force F_e, which needs to be sufficiently large to achieve numerical convergence and sufficiently small to remain in the linear response regime. As illustrated in the literature[50,52,54–56] as well as the example of ml-MoS_2 below, this balance is more readily achievable for materials with a high

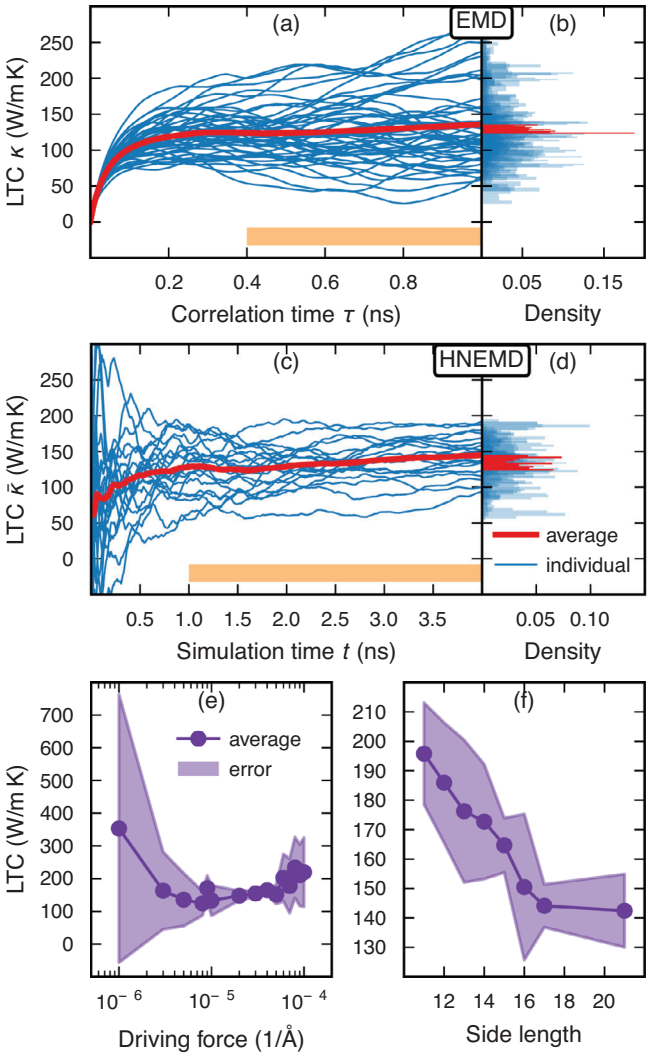

Figure 4. LTC of ml-MoS_2 at 300 K from a,b) EMD simulations according to Equation 3 and c,d) HNEMD simulations according to Equation 8 with $F_e^x = 4 \times 10^{-5}$ Å^{-1}. All simulations were based on the sixth-order model and used a $16 \times 16 \times 1$ supercell. a,c) The results from independent runs are shown by thin blue lines while the average is indicated by red thick lines. b,d) The histograms were generated by averaging the data after equilibration as indicated by the orange bars. Convergence of LTC from HNEMD simulations with e) driving force for a $15 \times 15 \times 1$ supercell and f) system size (side length in units of the ml-MoS_2 lattice constant) for $F_e^x = 4 \times 10^{-5}$ Å^{-1} based on the fourth-order model.

LTC, for which the HNEMD approach can yield a considerable reduction in computational effort compared to the EMD technique. The HNEMD furthermore allows one to conveniently extract the spectral decomposition of the LTC (see Equation 9 and **Figure 4**).

For the cases of ml-MoS_2 (Section 3.1) and $Ba_8Ga_{16}Ge_{30}$ (Section 3.2), we present results obtained using both EMD and HNEMD simulations, illustrating the points made above. This is done to demonstrate the *consistency* of the two approaches. We do *not* aim to provide an analysis of their respective efficiencies. We note, however, that while in the present case it appears that the two approaches are comparable in terms of computational effort, it is usually accepted that HNEMD simulations are more efficient, in particular for larger systems.

2.6. Thermal Conductivity from Boltzmann Transport Theory

For comparison, we also computed the LTC via the BTE. For ml-MoS_2 and SnSe we used both the relaxation time approximation (RTA) and the direct solution of the BTE described in ref. [57], both of which are implemented in Phono3py.[13] Calculations were carried out using the tetrahedron method for sampling the Brillouin zone with a $41 \times 41 \times 1$ $\boldsymbol{q}$-point mesh for ml-MoS_2 and a $16 \times 16 \times 16$ $\boldsymbol{q}$-point mesh for SnSe, which is the same mesh density as the one used in ref. [46].

For $Ba_8Ga_{16}Ge_{30}$, we employed the same approach and computational parameters as in ref. [22], using the ShengBTE code[15] with a $9 \times 9 \times 9$ $\boldsymbol{q}$-point mesh and a smearing parameter of 0.01, with the IFCs taken from ref. [35] as described above (Section 2.3).

3. Results and Discussion

3.1. Heat Conduction in ml-MoS_2

We start with a comparison of the EMD and HNEMD techniques. To obtain a bulk value for the LTC of this 2D material ml-MoS_2, we followed the common practice of assuming a finite sheet thickness corresponding to the layer spacing, using a value of 6.15 Å (see Table II in ref. [58]).

In the case of the EMD method, we ran 50 simulations each with a 1 ns equilibration and a 10 ns production period (**Figure 5**a,b), while in the case of the HNEMD method, we carried out 20 independent runs with a 1 ns equilibration and a 4 ns production period (Figure 5c,d). The two methods agree with each other up to the statistical error bounds, as shown in previous works using empirical potentials.[50,52,54–56] Since their statistical convergence behavior has already been analyzed in these references in detail, we do not carry out a further analysis of this aspect here. We emphasize, however, that both EMD and HNEMD require total simulation times exceeding many tens of nanoseconds to achieve well converged results, which is currently far beyond the reach of DFT calculations.

The HNEMD method requires one to choose a suitable value for the driving force that appears in Equation 6. To this end, we carried out a series of simulations at 300 K using $15 \times 15 \times 1$ supercells with driving forces in the range 10^{-6} Å^{-1} to 10^{-4} Å^{-1}. If the driving force is too small ($\lesssim 1 \times 10^{-5}$ Å^{-1}; Figure 5e) the statistical uncertainty becomes too large to obtain a meaningful LTC within the run time chosen for our MD simulations here. If, on the other hand, it is chosen too large ($\gtrsim 8 \times 10^{-5}$ Å^{-1}), one no longer observes the intrinsic LTC of the system but rather an overdriven response. In the intermediate region, however, one retrieves a consistent value for the LTC, which is independent of the driving forces and carries a small error bar. Based on this analysis, we chose a value of $F_e^x = 4 \times 10^{-5}$ Å^{-1} for the subsequent simulations for ml-MoS_2. It is important to emphasize that one can in principle choose any value for the driving force as long as it is below the threshold at which the response becomes nonlinear/overdriven (i.e., $< 8 \times 10^{-5}$ Å^{-1} in this case). The smaller the

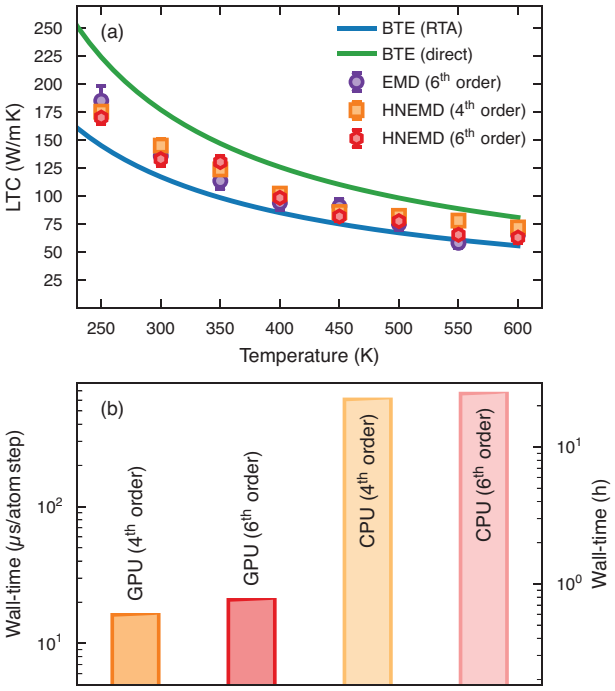

Figure 5. a) LTC of ml-MoS_2 as a function of temperature calculated using different approaches. b) Wall clock times for single MD runs (10^5 time steps), using GPUMD on an Nvidia Tesla P100 GPU and an Intel Core i7-4771 CPU, respectively.

driving force the longer the simulations are, however, required to achieve statistical convergence.

The next parameter of importance is the system size. Considering system sizes in the range 11 and 21, the LTC converges in fact rather slowly (Figure 5f) and only settles at a system size of about $16 \times 16 \times 1$, which is hence the size that was used for the subsequent simulations.

In general, both the optimal choice of the driving force and the system size can vary with temperature. In our experience this variation is, however, sufficiently small over the temperature range considered here, whence for the subsequent simulations, we used the same driving force and system size for all temperatures.

We can now consider the temperature dependence of the LTC (**Figure 6**a), limiting ourselves to temperatures above the Debye temperature to ensure that we remain in the classical regime. The results from EMD and HNEMD based on the sixth-order FCP agree within the error bars. The same can be said for the HNEMD results based on the fourth- and sixth-order FCPs, indicating that the higher-order terms in the IFC expansion play a minor role the LTC. In general the results are also in good agreement with experimental data.[59] Since the experimental measurements of the LTC exhibit considerable scatter in part due to the sensitivity of these materials to sample preparation, we do not discuss this comparison here further but refer the interested reader to, for example, refs. [58, 59].

It is, furthermore, instructive to compare the MD results with the LTC obtained via the BTE (Figure 6a). The LTC from RTA and the direct approach bound the MD data from below and above, respectively. It is established that the RTA typically underestimates the LTC for materials with intermediate to high conductivities.[15,57] Here, either approach includes, however, only phonon scattering up to third order. Fourth-order scattering processes lead to a renormalization of the phonon frequencies and also additional terms in the calculation of the phonon lifetimes. It is therefore a priori not clear whether they lead to an increase or decrease of the LTC relative to the third-order result. If renormalization is weak additional scattering processes should only decrease the LTC as observed, for example, ref. [7]. This is also the case here as the effect of temperature on the phonon spectrum of ml-MoS_2 is weak and the LTC from MD simulations, which are not limited in terms of scattering order, is lower than the LTC obtained via the direct solution of the BTE. This can be contrasted with the case of $Ba_8Ga_{16}Ge_{30}$ considered below (Section 3.2), for which the phonon renormalization is very strong and the opposite behavior is observed for the LTC.

Having demonstrated the predictive capability of the combination of FCPs with MD simulations, we can now consider the numerical efficiency of this approach (Figure 6b). A typical 100 ps FCP-MD simulation ($21 \times 21 \times 1$ unit cells or 1323 atoms) requires ≈1 day of wall clock time when run serially on a CPU (Intel Core i7-4771) using the implementation in HIPHIVE. By contrast, the same simulation requires only about 30 (fourth-order FCP) to 45 (sixth-order FCP) minutes on a GPU (Nvidia Tesla P100), corresponding to a speed-up of 30 to 40. We emphasize that this comparison is not entirely fair since high-performance GPUs are considerably more expensive and hence not as widely available as CPUs. Furthermore, parallelization of the CPU code can also improve performance. Nonetheless, the comparison provides a strong indication for the considerable advantages of GPU acceleration for FCP-MD simulations.

3.2. Heat Conduction in $Ba_8Ga_{16}Ge_{30}$

As noted above one of the distinct advantages of MD simulations is that they make no a priori assumption as to the heat conduction mechanism in the material and are therefore equally applicable to materials with high and low LTC. To demonstrate this explicitly, we now consider the inorganic clathrate $Ba_8Ga_{16}Ge_{30}$, a material with a very low LTC that exhibits strong phonon scattering and presents a considerable challenge for BTE approaches both due the size of the unit cell, complex ordering[41,60–62] and its very strong anharmonicity.[21,22,33] The latter requires one to account for phonon renormalization,for example, via self-consistent phonon theory[21] or temperature-dependent (effective) IFCs.[22] Since we have already established that the effect of isotope and disorder scattering is only appreciable below 10 K, they were not taking into account here.[22]

In the case of the EMD method, we ran 50 simulations each with a 1 ns equilibration and a 10 ns production period, while in the case of the HNEMD method, we carried out ten independent runs with a 1 ns equilibration and a 5 ns production period. To select a suitable driving force for the HNEMD simulations we ran tests at both 100 and 300 K (Figure S2a). This shows that suitable values for F_e^α fall between $\approx 2 \times 10^{-4}$ Å^{-1} and $\approx 6 \times 10^{-4}$ Å^{-1} regardless of temperature, supporting our earlier statement regarding the weak temperature dependence of suitable F_e^α choices. We emphasize that one should not choose

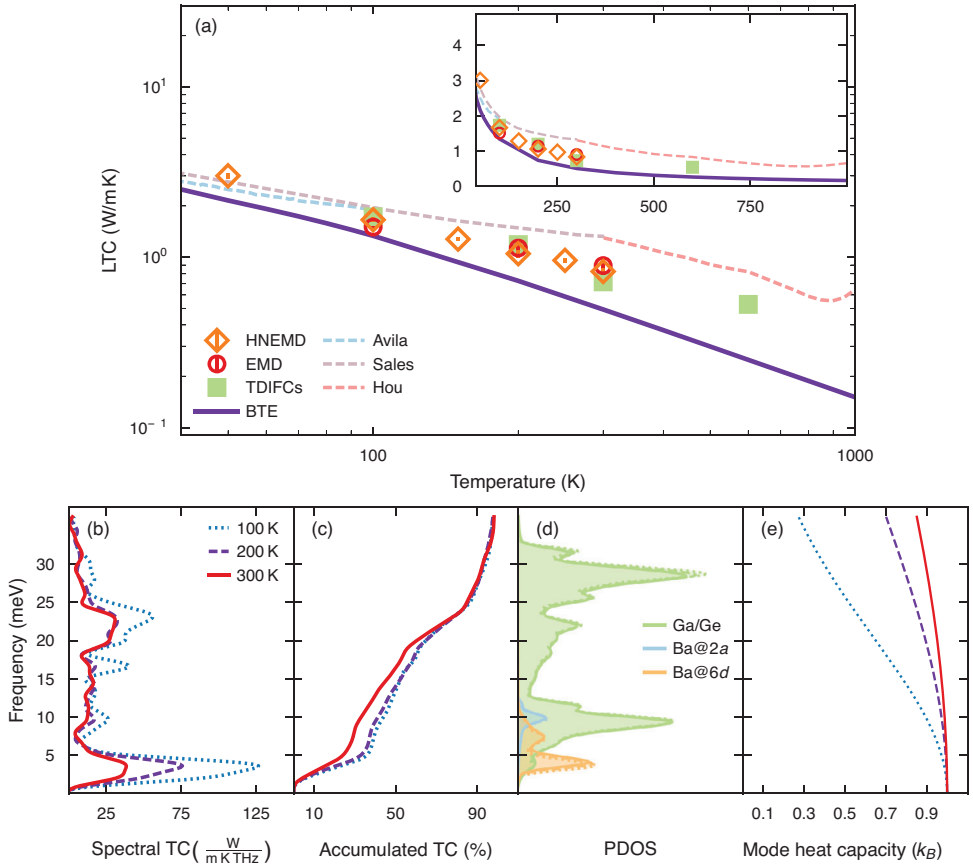

Figure 6. a) LTC of $Ba_8Ga_{16}Ge_{30}$ as a function of temperature from simulations, b) spectral decomposition according to Equation 9, c) relative integrated spectral thermal conductivity, d) phonon density of states (PDOS), and e) harmonic contribution to the heat capacity per mode for $Ba_8Ga_{16}Ge_{30}$. The inset in (a) shows the same data when using a linear scaling of the axes. The BTE, EMD, and HNEMD data have been obtained in the present work. The results based on temperature-dependent interatomic force constants (TDIFCs) are from Ref. [22] while the experimental data for single-crystalline n-type samples have been extracted from Refs. [63–65]

driving force values above $\approx 6 \times 10^{-4}$ Å^{-1} since they lead to a departure from the linear response regime. The lower limit is, however, dictated by statistical convergence and therefore can be always extended by running more and/or longer simulations. The lower threshold identified here is hence merely a choice of convenience.

We also carried out a convergence study of the system size, which shows the LTC to be rather sensitive to system size (Figure S2b). To obtain well-converged results one requires supercells comprising at least $5 \times 5 \times 5$ unit cells (6750 atoms) (Figure S2f). In our production runs, we therefore used $6 \times 6 \times 6$ supercells (11,664 atoms).

We can now inspect the temperature dependence of the LTC (Figure 4a). The HNEMD and EMD results are in close agreement with previous BTE calculations of the LTC, which used temperature-dependent IFCs.[22] In the latter case though, each data point required the generation of temperature-specific second- and third-order FCP, whereas the approach in the present work allows us to use a single fourth-order FCP for all temperatures.

The simulation results are also in good agreement with experiments on single-crystalline n-type samples,[63–65] improving over the "bare" third-order BTE results, which in agreement with earlier calculations[22,33] considerably underestimate the experimental LTC. The latter shortcoming can be related to the strong anharmonicity of this material, giving rise to considerable phonon renormalization, which needs to be taken into account, for example, via temperature-dependent IFCs[22] or self-consistent phonons.[21]

For the purpose of explaining the low LTC in $Ba_8Ga_{16}Ge_{30}$, we calculated its spectral decomposition according to Equation 9. One can distinguish four frequency regions (Figure 4b–e): i) Modes with frequencies $\lesssim$ 5 meV contribute between 25% and 40% of the total LTC with their importance diminishing with increasing temperature. ii) Modes between $\approx$5 meV and 20 meV contribute a further 25–30% to the total LTC. iii) Modes between $\approx$20 meV and 25 meV contribute about another 30% to the total LTC. v) The remaining small part of the LTC is associated with modes above 25 meV.

Most of the LTC thus stems from modes in the rather narrow regions (i) and (ii), which feature i) predominantly acoustic modes or ii) strongly dispersed optical modes with sizeable group velocities.[22] The contributions from regions (iii) and (iv) are small compared to the frequency range and PDOS in these

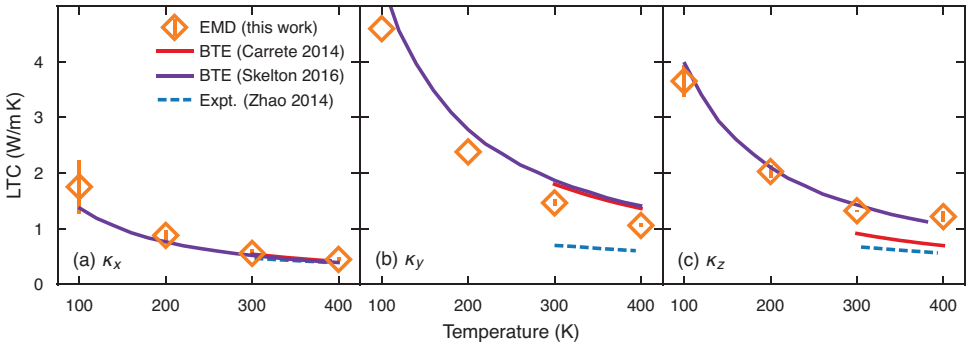

Figure 7. LTC of SnSe calculated using the EMD method (orange diamonds) based on a sixth-order FCP together with BTE calculations by Carrete et al.[66] (red solid line) and Skelton et al.[46] (purple solid line) as well as experimental measurements by Zhao et al.[68] (blue dashed line).

regions. This is due to these modes being strongly localized with very small group velocities.

The overall picture obtained is in semi-quantitative agreement with a similar analysis of BTE calculations based on temperature-dependent IFCs.[22] In the latter case, the differences between regions (i) and (iii) on one side and regions (ii) and (iv) on the other are, however, even more pronounced. We attribute this to the more comprehensive account for scattering mechanisms provided by the IFC-MD approach, which levels out the differences in particular in phonon lifetimes between the modes.

3.3. Heat Conduction in SnSe

As a last example, we consider the low-temperature structure (*Pnma*) of tin selenide (SnSe). This material has a LTC that is even smaller than that of $Ba_8Ga_{16}Ge_{30}$ and thanks to its very promising thermoelectric properties has received considerable attention in recent years. The LTC has been studied previously by BTE,[46,66] MD simulations using a ML potential[67] as well as experimentally[68] making it a good (yet challenging) system for benchmarking LTC calculation methods.

The harmonic (zero Kelvin) phonon dispersion obtained using the harmonic terms in oursixth-order FCP is in good agreement with previous theoretical studies (Figure S3), allowing for small differences arising from the choice of the XC functional, supercell size, and treatment of non-analytic corrections. There is a modest renormalization of the phonon dispersion (Figure S4) that mostly affects the optical branches, which shift downward by about 2 meV between 0 K and 500 K. The acoustic modes, on the other hand, hardly change in this temperature range.

For SnSe, we only employ the EMD method, using 40 independent simulations each with a 100 ps equilibration and a 1 ns production period for a system of size $4 \times 11 \times 11$ unit cells (3872 atoms) corresponding to an orthorhombic simulation cell with side lengths of about 50 Å in each direction.

Overall the LTC obtained via EMD simulations using the FCP are in very good agreement with both experiment[68] and earlier BTE calculations[46,66] (**Figure 7**). Similar to both experiment and the later BTE study[46] but in contrast to the earlier BTE study,[66] we do not find a strong difference in the LTC in the y and z directions. These results further demonstrate the applicability range of the present approach.

As note above, the temperature dependence of the phonon modes is weak (Figure S3), in particular for the acoustic modes that are the major carriers of heat. This suggests that the main reason for the very low LTC are short phonon-scattering lifetimes. Among the three materials considered here, SnSe is the most anharmonic (also see Section 3.4). It is therefore interesting to note that the BTE provides practically quantitative predictions for the LTC, already at the lowest applicable scattering order, that is, three-phonon scattering, and without taking into account phonon renormalization, in stark contrast to $Ba_8Ga_{16}Ge_{30}$ (Figure 4a). In fact, the temperature dependence of the LTC follows very closely the $1/T$ dependence observed for most crystalline thermal conductors, whereas for $Ba_8Ga_{16}Ge_{30}$ one obtains a relation closer to $1/\sqrt{T}$.[22,35]

A heuristic explanation is provided by the observation that the third-order IFCs are rather large and long ranged, as already noted in ref. [66]. They also contribute relatively more to the anharmonic terms of the energy and forces than in $Ba_8Ga_{16}Ge_{30}$ as discussed in the following section (**Figure 8**a,b).

3.4. Comparison of Degree of Anharmonicity

Since the FCPs used in this work are based on a systematic expansion of the energy in terms of increasing order, see Equation 1, it is possible to discriminate the contributions to energy and forces by order. This allows one in particular to quantify the level of anharmonicity present in different materials by averaging over snapshots generated by MD simulations, as demonstrated in ref. [69].

The decomposition of the total energy by order is straightforward and simply involves evaluating the individual terms in Equation 1 separately. One can then define the relative contribution to the potential energy χ_n due to terms of order n as

$$\chi_n = |V_n| / \sum_m |V_m| \tag{11}$$

The results reveal a clear ordering between the three materials considered in this study (Figure 8a). The most harmonic material, as expected, is ml-MoS_2 followed by $Ba_8Ga_{16}Ge_{30}$ and SnSe and the degree of anharmonicity quickly increases with temperature. A closer inspection of the contributions by order

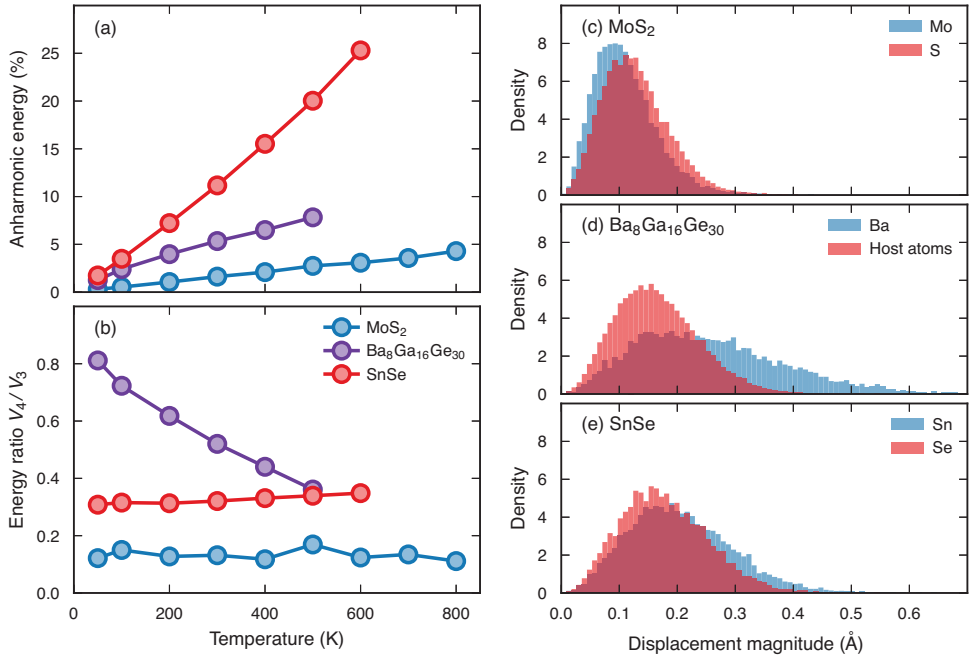

Figure 8. a) Anharmonic contributions to the energy in ml-MoS_2 (blue), $Ba_8Ga_{16}Ge_{30}$ (purple), and SnSe (red) calculated according to Equation 11. b) The ratio between the fourth-order energy and the third-order energy, E_4/E_3. c–e) Distribution of the magnitude of the atomic displacements, $\|u_i\|_2$, from MD simulations at 300 K.

sheds some light on the differences between $Ba_8Ga_{16}Ge_{30}$ and SnSe alluded to above. In the case of SnSe, the BTE with (non-renormalized) second- and third-order IFCs provides quantitative predictions for the LTC likely because the phonon frequencies are only weakly temperature dependent. This is consistent with the fourth-order contribution to the total energy V_4 being smaller than the third-order contribution V_3 (Figure 8b). In $Ba_8Ga_{16}Ge_{30}$ on the other hand, the fourth-order term is much more prominent, especially at low temperatures, translating to strong phonon renormalization, which needs to be taken into account when computing the LTC with third-order BTE.[21,22]

In this context it is also instructive to consider the magnitude of the atomic displacements (Figure 8c–e). The average displacements for SnSe are clearly larger than for ml-MoS_2, consistent with the softer phonons and higher anharmonicity of the former. $Ba_8Ga_{16}Ge_{30}$ presents a more intricate picture with the Ba "guest" atoms exhibiting a much broader and more extended distribution than the Ga and Ge atoms forming the host framework, an observation that is fully in line with the picture of the slightly undersized Ba atoms acting as rattlers in the cages provided by the host structure.

4. Conclusions

We have described and benchmarked a computational approach for accurate and efficient prediction of dynamical properties of materials in general and the LTC in particular. The approach uses a combination of the GPUMD and HIPHIVE codes, which are made available as free and open-source software. We thereby hope to encourage both the more widespread use of these techniques and their evolution through continuous and collaborative development.

The combination of FCPs and GPU-accelerated MD simulations has several distinct advantages. The construction of FCPs requires much less reference data and effort on behalf of the user than either ML or semi-empirical potentials. Yet they provide forces (and energies) of a precision very close to the underlying reference calculations (typically from DFT). As protocols for the generation of FCPs improve, reducing both the size of reference data sets and user input, this approach becomes increasingly attractive. There are potential drawbacks as FCPs can become unstable during MD simulations,[40] but as demonstrated in this paper by the example of SnSe such issue can be circumvented by (iteratively) including suitable configurations in the training process.

MD simulations for the calculation of dynamical properties, in particular the LTC, comprehensively account for phonon-scattering mechanisms and are readily applicable to the study of both high- and low-LTC materials. They can thereby circumvent some of the complications that arise when BTE calculations need to be carried out beyond three-phonon scattering processes and/or mode renormalization (temperature-dependent dispersion) is important. Limitations remain pertaining, for example, to the treatment of quantum effects, which can become important at low temperatures.

Here, we demonstrated the above points by applying the FCP-MD approach to a material with a moderate to high LTC (ml-MoS_2), and two materials with a very low LTC and strong phonon scattering ($Ba_8Ga_{16}Ge_{30}$ and SnSe). In all three cases, the underlying FCPs closely match reference DFT data (see, e.g., Figure 2) and the LTC from MD simulations match available reference data (Figures 6a, 4a, 7), while achieving very good computational efficiency (Figure 6b). By comparison with BTE calculations that include scattering processes up to third order, the MD results also

demonstrate the importance of higher-order scattering processes for quantitative calculations.

Finally, we have demonstrated the ability of MD simulations to provide additional insight on par with perturbative approaches, for example, via the PDOS and the spectral decomposition of the LTC (Figure 4b,c). We also note that much more extensive analyses can be readily carried out on the basis of MD trajectories, such as free energy calculations and time correlation functions, for example, via codes such as DYNASOR.[38]

Supporting Information

Supporting Information is available from the Wiley Online Library or from the author.

Acknowledgements

Funding from the Knut and Alice Wallenberg Foundation (2014.0226), the Swedish Research Council (2018-06482, 2020-04935), the Natural Science Foundation of China (No. 11974059), the Academy of Finland (QTF Centre of Excellence program No. 312298 and Academy Research Fellow funding No. 311058), the FLAG-ERA JTC-2017 project MECHANIC funded by the Swedish Research Council (VR 2017-06819) as well as the Danish Council for Strategic Research via the Programme Commission on Sustainable Energy and Environment through sponsoring of the project "CTEC – Center for Thermoelectric Energy Conversion" (project no. 1305-00002B) are gratefully acknowledged. The computations were enabled by resources provided by the Swedish National Infrastructure for Computing (SNIC) at NSC, PDC, and HPC2N partially funded by the Swedish Research Council through grant agreement no. 2018-05973. The authors also thank the CSC-IT Center for Science Ltd. and the Aalto Science-IT project for generous grants of computer time.

Conflict of Interest

The authors declare no conflict of interest.

Data Availability Statement

The results of the GPUMD calculations have been compiled in a set of data files. They are available as a Zenodo dataset [https://doi.org/10.5281/zenodo.5034182], which also contains examples of input files, including FCPs constructed with HIPHIVE and scripts for writing the latter in the format required by GPUMD.

Keywords

clathrates, force constant potentials, graphics processing unit acceleration, molecular dynamics, molybdenum disulfide, thermal conductivity

Received: June 26, 2021
Revised: October 2, 2021
Published online:

[1] H. Zhan, Y. Nie, Y. Chen, J. M. Bell, Y. Gu, *Adv. Funct. Mater.* **2020**, *30*, 1903841.
[2] Y. Zhao, Y. Cai, L. Zhang, B. Li, G. Zhang, J. T. L. Thong, *Adv. Funct. Mater.* **2020**, *30*, 1903929.
[3] Z. Chen, X. Zhang, Y. Pei, *Adv. Mater.* **2018**, *30*, 1705617.
[4] H. Song, J. Liu, B. Liu, J. Wu, H.-M. Cheng, F. Kang, *Joule* **2018**, *2*, 442.
[5] S. E. Kim, F. Mujid, A. Rai, F. Eriksson, J. Suh, P. Poddar, A. Ray, C. Park, E. Fransson, Y. Zhong, D. A. Muller, P. Erhart, D. G. Cahill, J. Park, *Nature* **2021**, *597*, 660.
[6] L. Lindsay, D. A. Broido, T. L. Reinecke, *Phys. Rev. Lett.* **2013**, *111*, 025901.
[7] S. Li, Q. Zheng, Y. Lv, X. Liu, X. Wang, P. Y. Huang, D. G. Cahill, B. Lv, *Science* **2018**, *361*, 579.
[8] F. Tian, B. Song, X. Chen, N. K. Ravichandran, Y. Lv, K. Chen, S. Sullivan, J. Kim, Y. Zhou, T.-H. Liu, M. Goni, Z. Ding, J. Sun, G. A. G. Udalamatta Gamage, H. Sun, H. Ziyaee, S. Huyan, L. Deng, J. Zhou, A. J. Schmidt, S. Chen, C.-W. Chu, P. Y. Huang, D. Broido, L. Shi, G. Chen, Z. Ren, *Science* **2018**, *361*, 582.
[9] K. Chen, B. Song, N. K. Ravichandran, Q. Zheng, X. Chen, H. Lee, H. Sun, S. Li, G. A. G. Udalamatta Gamage, F. Tian, Z. Ding, Q. Song, A. Rai, H. Wu, P. Koirala, A. J. Schmidt, K. Watanabe, B. Lv, Z. Ren, L. Shi, D. G. Cahill, T. Taniguchi, D. Broido, G. Chen, *Science* **2020**, *367*, 555.
[10] J. P. Heremans, V. Jovovic, E. S. Toberer, A. Saramat, K. Kurosaki, A. Charoenphakdee, S. Yamanaka, G. J. Snyder, *Science* **2008**, *321*, 554.
[11] T. Plirdpring, K. Kurosaki, A. Kosuga, T. Day, S. Firdosy, V. Ravi, G. J. Snyder, A. Harnwunggmoung, T. Sugahara, Y. Ohishi, H. Muta, S. Yamanaka, *Adv. Mater.* **2012**, *24*, 3622.
[12] M. Sajjad, Q. Mahmood, N. Singh, J. A. Larsson, *ACS Appl. Energy Mater.* **2020**, *3*, 11293.
[13] A. Togo, L. Chaput, I. Tanaka, *Phys. Rev. B* **2015**, *91*, 094306.
[14] T. Tadano, S. Tsuneyuki, *J. Phys. Soc. Japan* **2018**, *87*, 041015.
[15] W. Li, J. Carrete, N. A. Katcho, N. Mingo, *Comput. Phys. Commun.* **2014**, *185*, 1747.
[16] L. Paulatto, F. Mauri, M. Lazzeri, *Phys. Rev. B* **2013**, *87*, 214303.
[17] A. Chernatynskiy, S. R. Phillpot, *Comput. Phys. Commun.* **2015**, *192*, 196.
[18] J. Plata, P. Nath, D. Usanmaz, J. Carrete Montaña, C. Toher, M. Jong, M. Asta, M. Fornari, M. Buongiorno Nardelli, S. Curtarolo, *npj Comput. Mater.* **2017**, *3*, 45.
[19] Z. Han, X. Yang, W. Li, T. Feng, X. Ruan, Fourphonon: An extension module to shengbte for computing four-phonon scattering rates and thermal conductivity, arXiv:2104.04895, **2021**.
[20] B. Zhang, Z. Fan, C. Zhao, X. Gu, *J. Phys.: Condens. Matter* **2021**, *33*, 495901.
[21] T. Tadano, S. Tsuneyuki, *Phys. Rev. Lett.* **2018**, *120*, 105901.
[22] D. O. Lindroth, J. Brorsson, E. Fransson, F. Eriksson, A. Palmqvist, P. Erhart, *Phys. Rev. B* **2019**, *100*, 045206.
[23] L. Isaeva, G. Barbalinardo, D. Donadio, S. Baroni, *Nat. Commun.* **2019**, *10*, 3853.
[24] M. S. Green, *J. Chem. Phys.* **1954**, *22*, 398.
[25] R. Kubo, *J. Phys. Soc. Japan* **1957**, *12*, 570.
[26] D. J. Evans, *Phys. Lett. A* **1982**, *91*, 457.
[27] D. J. Evans, B. L. Holian, *J. Chem. Phys.* **1985**, *83*, 4069.
[28] C. Carbogno, R. Ramprasad, M. Scheffler, *Phys. Rev. Lett.* **2017**, *118*, 175901.
[29] S. Baroni, R. Bertossa, L. Ercole, F. Grasselli, A. Marcolongo, in *Handbook of Materials Modeling: Applications: Current and Emerging Materials* (Eds: W. Andreoni, S. Yip), Springer International Publishing, Berlin **2018**.
[30] K. Esfarjani, H. T. Stokes, *Phys. Rev. B* **2008**, *77*, 144112.
[31] K. Esfarjani, G. Chen, H. T. Stokes, *Phys. Rev. B* **2011**, *84*, 085204.
[32] F. Zhou, W. Nielson, Y. Xia, V. Ozoliņš, *Phys. Rev. Lett.* **2014**, *113*, 185501.
[33] T. Tadano, Y. Gohda, S. Tsuneyuki, *Phys. Rev. Lett.* **2015**, *114*, 095501.
[34] F. Eriksson, E. Fransson, P. Erhart, *Adv. Theory Simul.* **2019**, *2*, 1800184.
[35] E. Fransson, F. Eriksson, P. Erhart, *npj Comput. Mater.* **2020**, *6*, 135.

[36] F. Zhou, W. Nielson, Y. Xia, V. Ozoliņš, *Phys. Rev. B* **2019**, *100*, 184308.
[37] F. Zhou, B. Sadigh, D. Åberg, Y. Xia, V. Ozoliņš, *Phys. Rev. B* **2019**, *100*, 184309.
[38] E. Fransson, M. Slabanja, P. Erhart, G. Wahnström, *Adv. Theory Simul.* **2021**, *4*, 2000240.
[39] G. Eckold, *International Tables for Crystallography*, Vol. *D*, Wiley, New York **2004**, Ch. 2.1.
[40] A. Rohskopf, S. Wyant, K. Gordiz, H. Reza Seyf, M. Gopal Muraleedharan, A. Henry, *Comput. Mater. Sci.* **2020**, *184*, 109884.
[41] M. Ångqvist, D. O. Lindroth, P. Erhart, *Chem. Mater.* **2016**, *28*, 6877.
[42] G. Kresse, J. Hafner, *Phys. Rev. B* **1993**, *47*, 558.
[43] M. Dion, H. Rydberg, E. Schröder, D. C. Langreth, B. I. Lundqvist, *Phys. Rev. Lett.* **2004**, *92*, 246401.
[44] K. Berland, P. Hyldgaard, *Phys. Rev. B* **2014**, *89*, 035412.
[45] J. P. Perdew, K. Burke, M. Ernzerhof, *Phys. Rev. Lett.* **1996**, *77*, 3865.
[46] J. M. Skelton, L. A. Burton, S. C. Parker, A. Walsh, C.-E. Kim, A. Soon, J. Buckeridge, A. A. Sokol, C. R. A. Catlow, A. Togo, I. Tanaka, *Phys. Rev. Lett.* **2016**, *117*, 075502.
[47] Z. Fan, L. F. C. Pereira, H.-Q. Wang, J.-C. Zheng, D. Donadio, A. Harju, *Phys. Rev. B* **2015**, *92*, 094301.
[48] A. J. Gabourie, Z. Fan, T. Ala-Nissila, E. Pop, *Phys. Rev. B* **2021**, *103*, 205421.
[49] Z. Fan, L. F. C. Pereira, P. Hirvonen, M. M. Ervasti, K. R. Elder, D. Donadio, T. Ala-Nissila, A. Harju, *Phys. Rev. B* **2017**, *95*, 144309.
[50] K. Xu, Z. Fan, J. Zhang, N. Wei, T. Ala-Nissila, *Model. Simul. Mater. Sci. Eng.* **2018**, *26*, 085001.
[51] A. J. C. Ladd, B. Moran, W. G. Hoover, *Phys. Rev. B* **1986**, *34*, 5058.
[52] Z. Fan, H. Dong, A. Harju, T. Ala-Nissila, *Phys. Rev. B* **2019**, *99*, 064308.
[53] Z. Fan, W. Chen, V. Vierimaa, A. Harju, *Comput. Phys. Commun.* **2017**, *218*, 10.
[54] B. Dongre, T. Wang, G. K. H. Madsen, *Model. Simul. Mater. Sci. Eng.* **2017**, *25*, 054001.
[55] H. Dong, P. Hirvonen, Z. Fan, T. Ala-Nissila, *Phys. Chem. Chem. Phys.* **2018**, *20*, 24602.
[56] K. Xu, A. J. Gabourie, A. Hashemi, Z. Fan, N. Wei, A. B. Farimani, H.-P. Komsa, A. V. Krasheninnikov, E. Pop, T. Ala-Nissila, *Phys. Rev. B* **2019**, *99*, 054303.
[57] L. Chaput, *Phys. Rev. Lett.* **2013**, *110*, 265506.
[58] D. O. Lindroth, P. Erhart, *Phys. Rev. B* **2016**, *94*, 115205.
[59] P. Jiang, X. Qian, X. Gu, R. Yang, *Adv. Mater.* **2017**, *29*, 1701068.
[60] M. Christensen, S. Johnsen, B. B. Iversen, *Dalton Trans.* **2010**, *39*, 978.
[61] M. Ångqvist, P. Erhart, *Chem. Mater.* **2017**, *29*, 7554.
[62] J. Brorsson, Y. Zhang, A. E. C. Palmqvist, P. Erhart, *Chem. Mater.* **2021**, *33*, 4500.
[63] M. Avila, K. Suekuni, K. Umeo, T. Takabatake, *Physica B: Condens. Matter* **2006**, *383*, 124.
[64] B. C. Sales, B. C. Chakoumakos, R. Jin, J. R. Thompson, D. Mandrus, *Phys. Rev. B* **2001**, *63*, 245113.
[65] X. Hou, Y. Zhou, L. Wang, W. Zhang, W. Zhang, L. Chen, *J. Alloys Comp.* **2009**, *482*, 544.
[66] J. Carrete, N. Mingo, S. Curtarolo, *Appl. Phys. Lett.* **2014**, *105*, 101907.
[67] H. Liu, X. Qian, H. Bao, C. Y. Zhao, X. Gu, *J. Phys.: Condens. Matter* **2021**, *33*, 405401.
[68] L.-D. Zhao, S.-H. Lo, Y. Zhang, H. Sun, G. Tan, C. Uher, C. Wolverton, V. P. Dravid, M. G. Kanatzidis, *Nature* **2014**, *508*, 373.
[69] F. Knoop, T. A. R. Purcell, M. Scheffler, C. Carbogno, *Phys. Rev. Mater.* **2020**, *4*, 083809.
[70] J. Brorsson, A. Hashemi, Z. Fan, E. Fransson, F. Eriksson, T. Ala-Nissila, A. V. Krasheninnikov, H.-P. Komsa, P. Erhart, Data and code for "Efficient calculation of the lattice thermal conductivity by atomistic simulations with ab-initio accuracy," **2021**. https://doi.org/10.5281/zenodo.5034182 (accessed: November 2021).